31

# Carbon Nanotube-Nanoparticle Hybrid Structures

Junhong Chen[1,2] and Ganhua Lu[1]
[1]*University of Wisconsin-Milwaukee*
*U.S.A.*
[2]*Tongji University*
*P. R. China*

## 1. Introduction

The discovery of carbon nanotubes (CNTs) (Iijima 1991; Iijima & Ichihashi 1993) has inspired extensive research activities unprecedented in nanoscience and nanotechnology. CNTs are very versatile due to their small diameter, high aspect ratio (Zheng et al. 2004), great structural integrity (Hinds et al. 2004; Jung et al. 2006), high electrical (Kang et al. 2007) and thermal conductivity (Berber et al. 2000), remarkable thermal (Kim et al. 2004) and chemical stability (Liu et al. 1999), and exceptional strength and resilience (Treacy et al. 1996; Saito 1998; Yu et al. 2000). Nanoparticles (NP) with sizes between 1 and 100 nm have attracted considerable interest because of their unique electronic, optical, magnetic, mechanical, and chemical properties that differ from those of both their constituent atoms/molecules and their corresponding bulk materials. CNTs decorated with NPs form a new class of hybrid nanomaterials that could potentially display not only the unique properties of NPs (Fissan et al. 2003; Scher et al. 2003) and nanotubes (Dresselhaus et al. 2001; de Heer 2004; Dresselhaus 2004), but also additional novel physical and chemical properties due to the interaction between CNTs and attached NPs. These hybrid nanomaterials have recently been shown as promising building blocks for various applications, including gas sensors (Kong et al. 2001; Sun & Wang 2007; Lu et al. 2009), fuel cells (Mu et al. 2005; Kongkanand et al. 2006; Robel et al. 2006), solar cells (Landi et al. 2005; Guldi et al. 2006; Kongkanand et al. 2007; Lee et al. 2007), Li-ion batteries (Zhang et al. 2006), hydrogen storage (Yildirim & Ciraci 2005; Anson et al. 2006), and transparent conductive electrodes (Kong et al. 2007).

This chapter begins by outlining the significance of CNT-NP hybrid structures in terms of materials advantages and potential applications. Then, we introduce the assembly of various metallic and semiconducting NPs onto the external surfaces of CNTs via the electrostatic force directed assembly (ESFDA) process that we have recently developed. Single-walled CNTs (SWCNTs), multiwalled CNTs (MWCNTs), randomly dispersed CNTs, and well-aligned CNT arrays can be decorated with a broad range of NPs (including both aerosol and colloidal NPs) through the ESFDA process for the generation of CNT-NP hybrid

[1] all correspondence should be addressed to jhchen@uwm.edu or 1-414-229-2615.

structures. Important factors that control the synthesis of the CNT-NP hybrid structures will be discussed for the ESFDA method. Fundamental understanding of the binding mechanism between CNTs and NPs will facilitate the rational design and use of these novel hybrid structures. The chapter also discusses the structure evolution of an example CNT-NP system under successive annealing cycles, attempting to shed light onto the interaction between the NP and the CNT. The chapter ends with a novel gas-sensing platform based on CNT-NP structures to illustrate the potential applications of such hybrid nanostructures.

## 2. CNT-NP: A New Class of Multifunctional Nanomaterials

Decorating CNTs with NPs has been one of the most intensively studied areas in the past decade (Georgakilas et al. 2007). These NP-loaded CNTs, regarded as a new class of multifunctional nanomaterials, are highly promising for widespread applications due to several materials advantages. Heterojunctions formed at the interface of the NP and the CNT can have an unusually minute junction area (less than 10 $nm^2$) and provide opportunities to tune the size, shape, and chemistry, and thus material properties (Peng et al. 2009). Electron transfer across the NP-CNT junction could be very sensitive to surrounding molecular species and photon illumination. In addition, CNTs can serve as a robust support for the dispersion and stabilization of NPs, which explains the enormous effort in the use of CNT-NP structures for catalysis.

The CNT-NP hybrid structure has been demonstrated as a new gas-sensing platform. For example, Pd-CNT systems have been used for $H_2$ detection with CNTs as a transducer and amplifier to convert the chemical reaction between Pd and $H_2$ into strong electrical signals. Kong et al. demonstrated that individual SWCNTs, as well as SWCNT networks, show enhanced $H_2$ sensing capability after being decorated with Pd NPs (Kong et al. 2001); the resistance of a single-SWCNT (semiconducting) device doubled upon exposure to 400 ppm $H_2$. Sun et al. fabricated flexible $H_2$ sensors on plastic substrates using necklace-like structures of Pd NPs electrochemically deposited on SWCNT networks (Sun & Wang 2007). MWCNTs decorated with discrete $SnO_2$ NPs showed room-temperature gas sensing capability for low concentration gases ($H_2$, CO, and $NO_2$) diluted in air (Lu et al. 2009).

In fuel cells, the catalytic activity of metal NPs for the electro-oxidation of fuel molecules strongly depends on the size and the shape of NPs (Valden et al. 1998), the type of catalyst support (Wolf & Schuth 2002), and the method of catalyst preparation (Liu et al. 1999). CNTs are considered to be strong candidates for catalyst support because of their high surface-to-volume ratio, stability, and unique mechanical properties (Treacy et al. 1996; Saito 1998; Yu et al. 2000). NPs with uniform sizes loaded onto CNTs have been proven effective for catalyzing redox reactions because of the increased surface area and the improved electrocatalytic activity (Kongkanand et al. 2006; Shao et al. 2009).

CNTs coated with CdSe and CdS NPs have been demonstrated for potential solar cell applications (Landi et al. 2005; Robel et al. 2005), in which semiconductor NPs are photoreceptors and CNTs are interconnects for conducting electrons from the photoexcitation of the semiconductor nanocrystals. The hydrogen storage capacity of Pd NPs has been shown to increase when they are supported on CNTs instead of raw carbon materials (Anson et al. 2006) due to the maximized active surface of Pd NPs on CNTs and the possible spread of $H_2$ from the Pd structure to CNTs (known as the hydrogen spillover effect (Conner & Falconer 1995)). Finally, it has been demonstrated both experimentally

(Kong et al. 2007) and theoretically (Khoo & Chelikowsky 2009) that the electrical conductivity of SWCNT can be improved by decorating metallic NPs, which can be attributed to a doping-induced electron depletion mechanism.

## 3. Synthesis of CNT-NP Hybrid Structures

Unsurprisingly, the synthesis of CNT-NP hybrid structures has attracted growing interest and a number of methods to produce CNT-NP structures have emerged in recent years. These methods can be broadly divided into two categories: wet-chemistry methods and dry routes. Most wet-chemistry methods involve the chemical functionalization of the CNT surface followed by the assembly of nanocrystals onto the CNTs via covalent (Zamudio et al. 2006), noncovalent (Li et al. 2006), or electrostatic interactions (Kim & Sigmund 2004; Xing 2004). Comprehensive reviews on chemical synthesis methods of CNT-NP hybrid structures have been carried out by Georgakilas et al. (Georgakilas et al. 2007) and Peng et al. (Peng et al. 2009). Here, we focus on a facile dry method, referred to as electrostatic force directed assembly (ESFDA), recently developed in our laboratory.

### 3.1 Electrostatic force-directed assembly for CNT-NP structure synthesis

The ideal technique for synthesizing a CNT-NP hybrid structure should be, in general, suitable for the deposition of NPs of a wide range of materials (metallic and semiconducting) onto CNTs with different morphologies (randomly dispersed or well-aligned). The electrostatic force directed assembly (ESFDA) is such a scalable technique, which can assemble nearly any electrically-charged aerosol NPs onto CNTs for synthesizing CNT-NP hybrid nanostructures and fabricating multifunctional devices. By taking advantage of the extremely small diameter of CNTs (Dresselhaus et al. 2001), a locally enhanced electric field in the neighborhood of CNTs can be generated, which is then used to direct the assembly of charged aerosol NPs onto the external surface of both random CNTs and vertically-aligned CNTs (or CNT arrays) (Huang et al. 1998).

A schematic diagram of the ESFDA process is shown in Fig. 1. The aerosol NPs were produced through physical vaporization of solid precursor materials using the mini-arc plasma source sustained between a tungsten cathode and a graphite anode (Chen et al. 2007). A fraction of the produced NPs was charged by the arc plasma or through thermionic emission, which made the ESFDA feasible without additional NP charging devices. These NPs were carried by room-temperature gases into a gap between two electrodes to form a stagnation flow (Q). One electrode is the grounded metal tubing that introduces the aerosol NPs; the other electrode, which is applied with a direct current (dc) voltage (V), was fabricated by dispersing CNTs onto a holey-carbon-coated copper grid. The gap distance (D) between the two electrodes was maintained with a precision-machined ceramic spacer. The nanotubes used in the experiment include both SWCNTs and MWCNTs. Surfactants have been used to disperse CNTs in DI water for more uniform coating; however, controlled experiments with pristine CNT powders and CNTs dispersed with surfactants have shown that the coating process relies on the electric field rather than the surfactants. Without the dc voltage / electric field, the NPs followed the gas flow perfectly and no particles were observed on the CNTs. With a dc voltage applied to the copper grid, the electric field near the CNT surface was significantly enhanced and both pristine and dispersed CNTs were successfully coated with NPs.

The field enhancement was facilitated by suspending CNTs on either a holey-carbon-coated copper grid or a bare copper grid. This was evidenced by significantly higher assembly efficiency with the aforementioned two grids than the carbon-coated copper grid without holes for the same operating conditions. NPs have also been observed at the edges of carbon holes and grid bars, where the electric field is highly enhanced. Two values of gap distance (0.5 and 2 mm) were used in the experiment. A lower voltage was needed to achieve the same assembly for a smaller gap. With the gap distance reduced from 2 to 0.5 mm, the required voltage decreased from 2 kV to 500 V. Based on our calculations, the maximum electric field near the surface of a 20-nm-diameter CNT reaches $2.45\times10^6$ V/m for V = 2 kV and D = 2 mm. The maximum electric field possible for the assembly is limited by the breakdown field of the carrier gas, e.g., about $3\times10^6$ V/m for dry air (Chen & Davidson 2003).

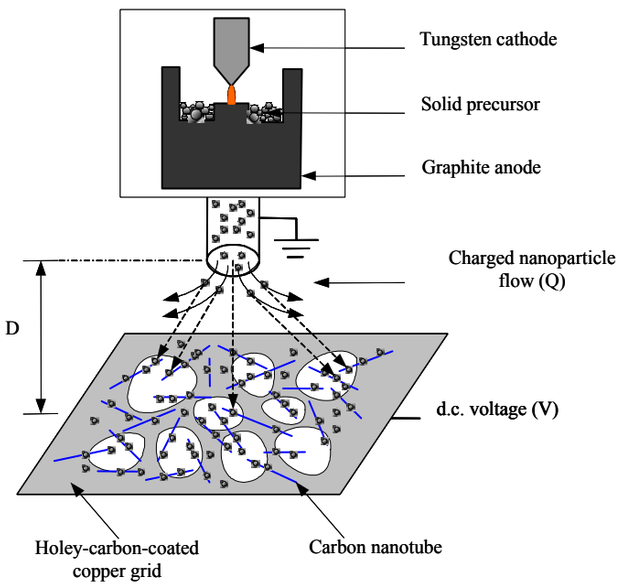


Fig. 1. Electrostatic force directed assembly (ESFDA) process. The locally enhanced electric field near CNTs results in a directed assembly of charged aerosol NPs onto CNTs. Reprinted with permission from (Chen & Lu 2006). Copyright 2006 IOP

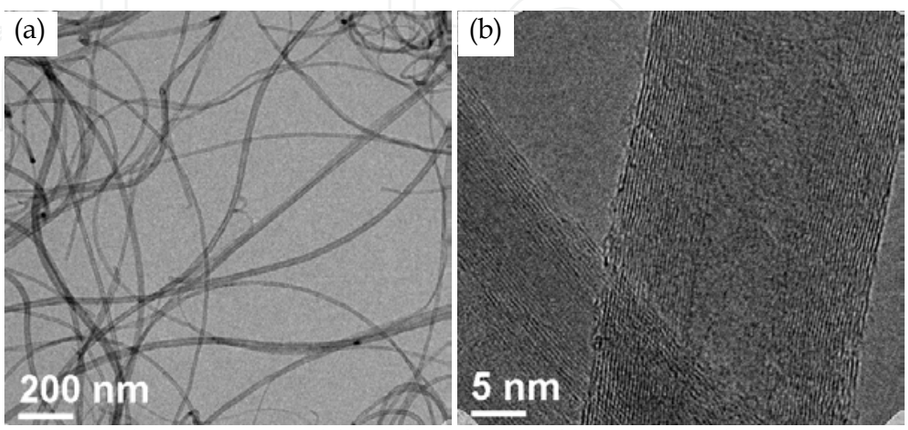


Fig. 2. Low-magnification TEM (a) and HRTEM (b) images of MWCNTs before NP assembly. Reprinted with permission from (Zhu et al. 2008). Copyright 2008 ASME

The successful assembly of NPs onto CNTs is confirmed by low-magnification transmission electron microscopy (TEM) and high-resolution TEM (HRTEM) images. As a comparison, Fig. 2 (a) shows the TEM image of MWCNTs before assembly, with a diameter of about 20-40 nm and a length of several micrometers. It is obvious that the MWCNT surface is very smooth, which can be further confirmed by the corresponding HRTEM image (Fig. 2(b)).
To demonstrate the material independence of ESFDA, NPs of semiconductor tin oxide ($SnO_2$) and metallic silver (Ag) were assembled onto both MWCNTs and SWCNTs. These composite structures were obtained at room temperature and atmospheric pressure with an assembly time (t) of 5.5 min. NPs have been found on both the outside wall and the tip of nanotubes. Figure 3(a) shows a representative TEM image of as-prepared MWCNTs coated with $SnO_2$ NPs. The ESFDA technique clearly shows the potential for efficient, large-scale decoration of CNTs with NPs. It can be seen that nonagglomerated $SnO_2$ NPs are quite uniformly distributed on the MWCNT surface. The hybrid structure can be more clearly seen from the HRTEM image shown in Fig. 3(b), with $SnO_2$ NPs less than 5 nm. Both the nonagglomerated entity and the crystallinity of NPs were preserved after the assembly. The measured lattice fringes of 0.26 and 0.33 nm correspond to the (101) and (110) crystal planes of rutile $SnO_2$, respectively. In principle, uncapped metal NPs tend to agglomerate even at room temperature. The nonagglomerated entity of NPs preserved during the assembly is likely attributed to the predominant unipolar charges carried by these NPs before reaching CNTs. The unipolar charges effectively prevent the NPs from agglomeration.

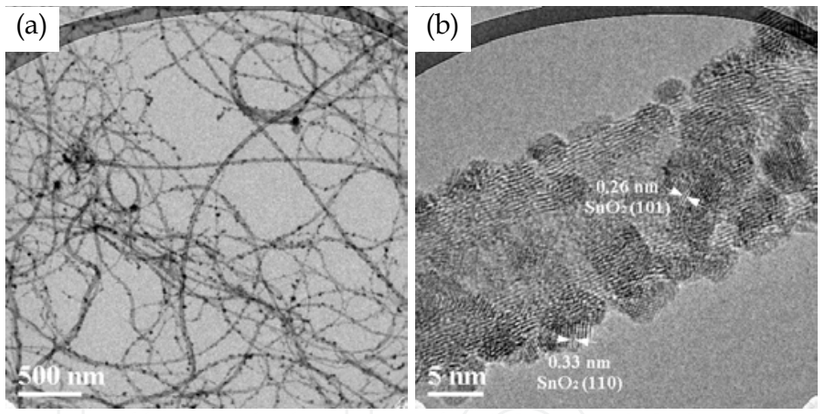


Fig. 3. (a) TEM image of large-scale decoration of MWCNTs with $SnO_2$. (b) HRTEM image of an MWCNT coated with $SnO_2$ NPs. (Operating conditions: D=2 mm, Q= 5.15 lpm, V=-2 kV, and t=5.5 min) Reprinted with permission from (Chen & Lu 2006). Copyright 2006 IOP

Similar results have been obtained for Ag NPs. Relatively uniform coverage of Ag NPs on MWCNTs is observed in Fig. 4(a). The HRTEM image of Fig. 4(b) clearly resolves the presence of Ag nanocrystals with sizes less than 10 nm. The lattice fringes of 0.23 and 0.20 nm correspond to the (111) and (200) planes of Ag crystal, respectively.
NPs of Ag and $SnO_2$ have also been successfully assembled onto SWCNTs using the ESFDA technique, although a significant fraction of the SWCNTs is semiconductive. Due to the strong van der Waals force between SWCNTs, small bundles instead of individual SWCNTs have been obtained after dispersion for the coating. The HRTEM images of coated SWCNT bundles are shown in Figs. 5(a) and (b) for $SnO_2$ and Ag, respectively. The lattice fringe of 0.33 nm shown in the HRTEM image of Fig. 5(a) corresponds to the (110) plane of rutile $SnO_2$, confirming the

successful assembly of $SnO_2$ nanocrystals onto SWCNTs. Similarly, the HRTEM image of Fig. 5(b) displays the lattice fringes of 0.23 nm corresponding to the (111) plane of Ag.

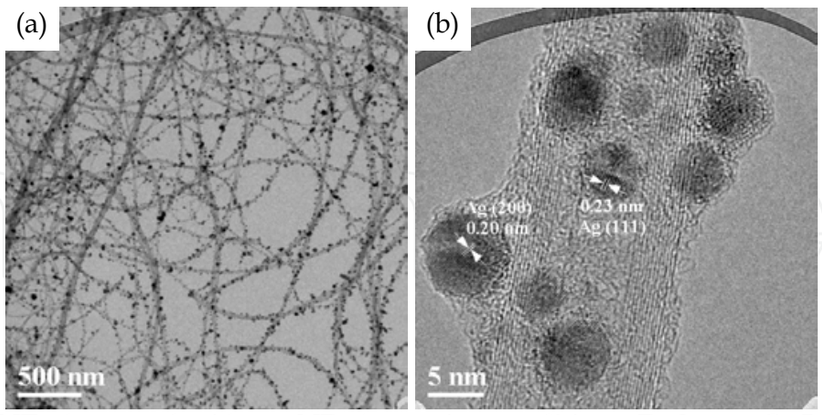


Fig. 4. MWCNTs decorated with Ag NPs (operating conditions: D=2 mm, Q=5.15 lpm, V=-2 kV, and t= 5.5 min). (a) TEM and (b) HRTEM images of Ag NP-MWCNT structure. Reprinted with permission from (Chen & Lu 2006). Copyright 2006 IOP

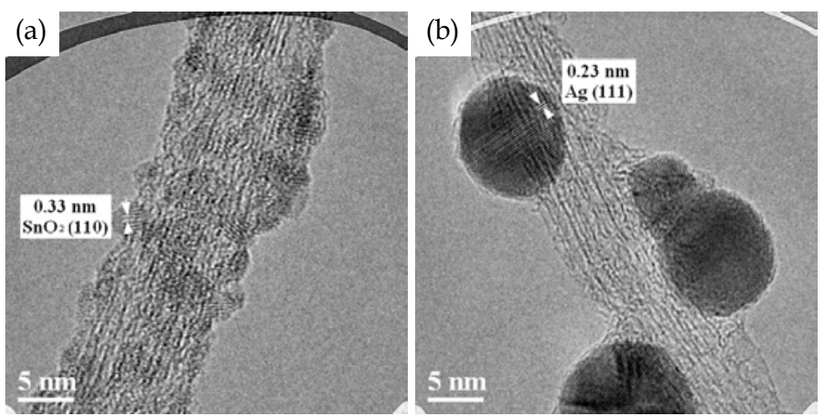


Fig. 5. HRTEM images of SWCNT bundle decorated with $SnO_2$ (a) and Ag (b) NPs (operating conditions: D = 2 mm, Q = 5.15 lpm, V = -2 kV, and t = 5.5 min). Reprinted with permission from (Chen & Lu 2006). Copyright 2006 IOP

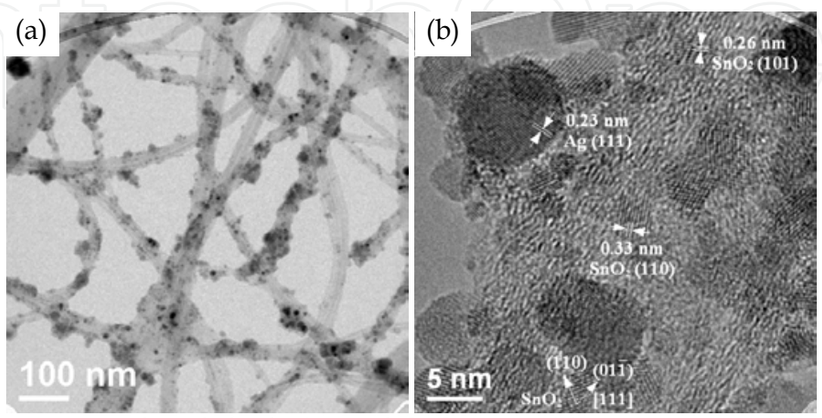


Fig. 6. MWCNTs coated with both Ag and $SnO_2$ NPs: (a) Low-mag. TEM image and (b) HRTEM image. Reprinted with permission from (Zhu et al. 2008). Copyright 2008 ASME

Due to the material independence of ESFDA, the range of NP materials for the assembly has been greatly expanded. As shown in Fig. 6, MWCNTs have been sequentially coated with $SnO_2$ and Ag nanocrystals. Figure 6(a) shows the low magnification TEM image of the double-component NP-coated MWCNTs. The uniformity of the NP coverage is not as good as that in the single-component NP-CNT sample. The HRTEM image in Fig. 6(b) provides more detailed information of the interesting hybrid structure. The lattice fringes of Ag and $SnO_2$ nanocrystals show simultaneously on the same MWCNT.

### 3.2 Size selection in the ESFDA process

The relatively broad size distribution of as-produced NPs from the mini-arc source made it possible to observe the NP size selection during the assembly. The size distribution of tin oxide NPs docking on MWCNTs (Fig. 3(a)) was measured using TEM and is shown in Fig. 7. Compared with the as-produced NPs before assembly (inset of Fig. 7, mean diameter $\overline{D}_p$ = 14.1 nm, standard deviation σ = 8.2 nm), the assembled NPs on nanotubes were much smaller ($\overline{D}_p$ = 2.9 nm) and the particle size distribution was much narrower (σ = 1.0 nm). This implies that there was an intrinsic size selection during the assembly process. The size selection feature of ESFDA is very attractive for many applications and it relaxes the requirement for the NP production process, particularly when the state-of-the-art aerosol classifiers are facing resolution challenges in the lower nanometer size range.

For the stagnation flow shown in Fig. 1, NPs migrate along the electric field lines while being carried away by the gas flow. NPs reaching CNTs are selected through their electrical mobility ($Z_p = v_p / E = (neC_c)/(3\pi\mu D_p)$) (Seinfeld & Pandis 1998), the ability of a particle to move in an electric field, where $v_p$ is the NP velocity along electric field lines, E is the electric field, n is the number of elementary charges carried by nanoparticles, e is the elementary charge, $C_c$ is the Cunningham slip correction factor, and μ is the flow viscosity). Only small NPs with sufficient electrical mobility can be assembled onto CNTs for a given electric field strength and flow residence time. Larger NPs with smaller electrical mobility remain in the stagnation flow and are carried away by the flow.

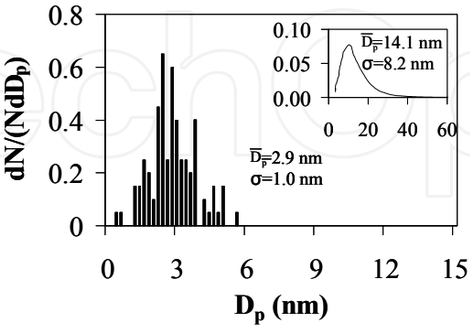


Fig. 7. $SnO_2$ NP size distribution before (shown in the inset) and after the assembly (operating conditions: D = 2 mm, Q = 5.15 lpm, V = -2 kV, and t = 5.5 min). Reprinted with permission from (Chen & Lu 2006). Copyright 2006 IOP

### 3.3 Control over the ESFDA process

The ESFDA has considerable control over the assembly process. The areal density of NPs on CNTs can be easily controlled by adjusting the assembly time for a given NP concentration (Fig. 8). As expected, the areal density increased with increasing assembly time. The entire external surface of CNTs may be coated with NPs if the assembly time is sufficiently long.

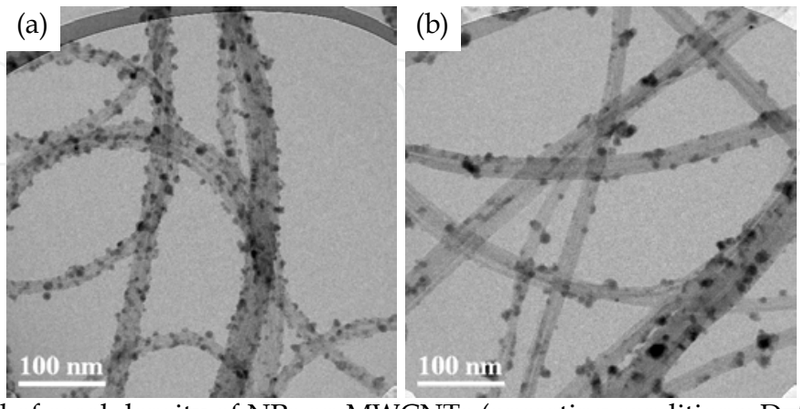


Fig. 8. Control of areal density of NPs on MWCNTs (operating conditions: D=2 mm, Q=5.15 lpm, V=-2 kV). TEM images of MWCNTs coated with $SnO_2$ NPs for (a) t=5.5 and (b) 2.75 min, respectively. Reprinted with permission from (Chen & Lu 2006). Copyright 2006 IOP

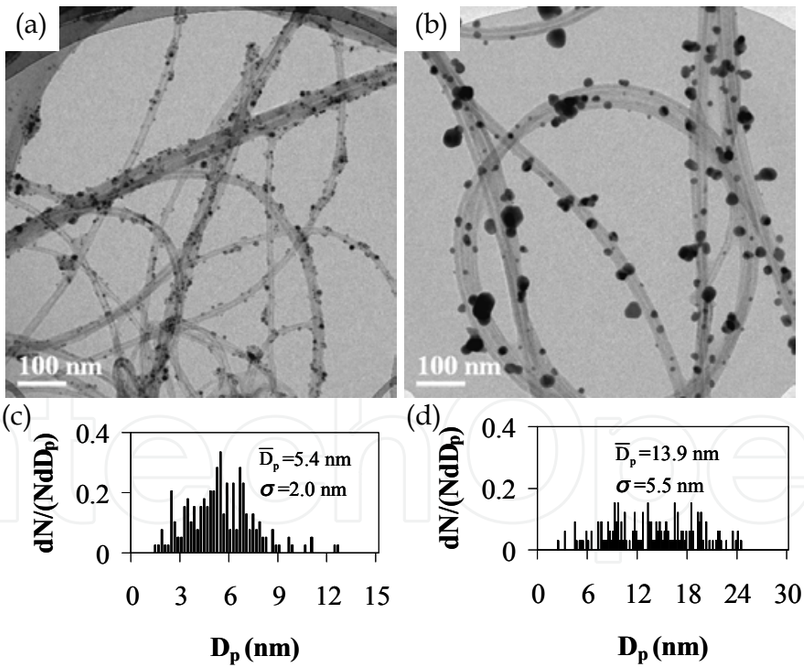


Fig. 9. Control of size distribution of Ag NPs on MWCNTs during the assembly by varying flow rate Q (operating conditions: D=2 mm, V=-2 kV, and t=5.5 min). (a) and (b), TEM images of MWCNTs coated with Ag NPs for Q=5.15 and 2.15 lpm, respectively. (c) and (d), size distribution of Ag NPs on CNTs shown in (a) and (b), respectively. Reprinted with permission from (Chen & Lu 2006). Copyright 2006 IOP

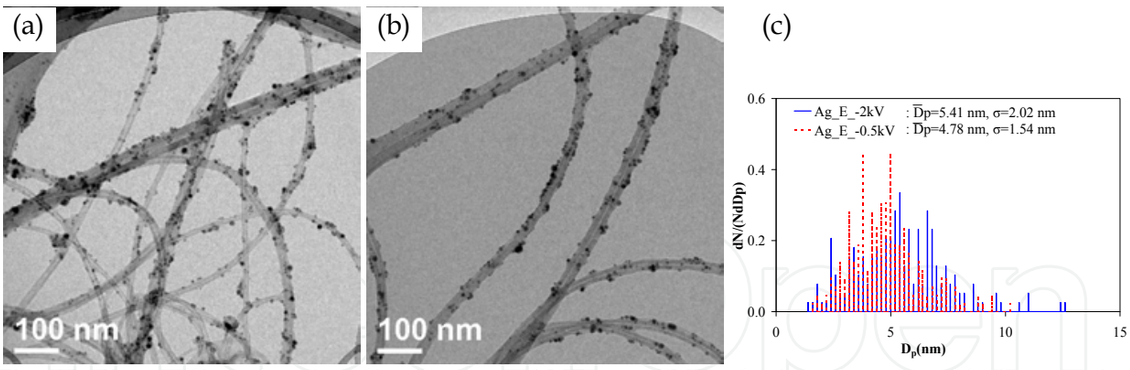


Fig. 10. Controlling the size distribution of NPs on CNTs during the assembly by varying electric field (operating conditions: D = 2 mm, Q = 5.15 lpm, and t = 5.5 min). (a) and (b), TEM images of MWCNTs coated with Ag NPs for V = -2 kV and -0.5 kV, respectively. (c) comparison of the size distributions of Ag NPs on CNTs shown in (a) and (b).

For polydisperse aerosol NPs, the size distribution of NPs on CNTs can be controlled by the aerosol flow rate and the electric field, along with the intrinsic size selection during the assembly process. With the decrease of aerosol flow rate, flow residence time increased and larger particles with smaller electrical mobility assembled onto CNTs for a fixed electric field (Fig. 9). Similar control over the particle size distribution has also been achieved by varying the electric field (Fig. 10). With the increase of electric field, larger particles with smaller electrical mobility assembled onto CNTs. The control of NP size on nanotubes is desirable since NP properties can be tuned with the particle size (Alivisatos 1996).

### 3.4 Assembly of NPs onto Vertically Aligned CNTs

Vertically-aligned CNTs are of great interest for practical device applications due to the potential for higher device efficiency and packing density. For instance, in fuel cells with metal catalyst nanocrystals coated on CNTs, the nature of loosely packed CNT powders could substantially decrease the effective contact area between nanocrystals and reactants, thereby decreasing the metal catalytic activity. Substituting loose CNT powders with aligned CNTs could overcome the disadvantage and increase the fuel cell efficiency.

While wet-chemistry methods work well with randomly dispersed CNTs, they are not suitable for vertically aligned CNTs—wet processing damages the aligned structure, as the upper ends of the neighboring nanotubes have been observed to bundle together and some nanotubes are caused to lie down (Ye et al. 2005). On the other hand, the ESFDA process, as a dry route, is considered suitable for producing CNT-NP structures without damaging the aligned arrangement of the CNT array. During the ESFDA process, the random CNTs must be suspended in order to maximize the electric field enhancement, which is critical to the assembly. The use of vertically-aligned CNTs represents another means to realize the field enhancement.

Figure 11 shows a schematic diagram of the process to coat a CNT array with aerosol NPs. Silver nanocrystals were carried by an inert carrier gas ($Ar/N_2$) and delivered into an electrode gap to form a stagnation flow. The top electrode was a grounded metal tube that introduced the aerosol nanocrystals. The bottom electrode was a Si wafer with vertically-aligned MWCNTs that had previously grown on it, and it was electrically biased with a constant voltage (-2 kV). The gap distance (D) between the two electrodes was about 2 mm.

With the bias voltage applied to the aligned MWCNTs on the Si wafer, the electric field near the MWCNT surface was significantly enhanced, especially at the tips, and the oppositely-charged Ag nanocrystals were attracted onto the surfaces of the MWCNTs.

The assembly of nanocrystals onto the CNT array is demonstrated by scanning electron microscopy (SEM) and TEM images. As a comparison, Figs. 12(a) and (b) show the SEM images of as-grown, vertically-aligned MWCNTs on an Si wafer. The CNTs were about 10 μm in length and 150 nm in diameter. The average spacing between nanotubes was about 500 nm, with an estimated areal density of $4\times10^8$ tubes/cm$^2$. A catalyst particle containing Ni caps the tip of each CNT, preventing the nanocrystals from assembling onto the interior surface of the CNTs. The external surface of the CNTs appears smooth with no particles observed. Figure 12(c) shows an MWCNT array coated with Ag NPs. The Ag NPs are distributed on the outside surfaces of the CNTs, particularly on the upper portion of the aligned MWCNTs due to the strong field enhancement effect close to the tips. Evidence of these NPs is better resolved in the higher magnification SEM image shown in Fig. 12(d).

Figure 13(a) shows a typical low-magnification TEM image of the Ag NP-MWCNTs that were transferred onto a TEM grid after being scratched off the Si wafer. Both the NP areal density and the average NP size maximize at the CNT tip, consistent with the SEM observation (Fig. 12(d)). The CNT in Fig. 13(a) bears a bamboo structure, typically from the PECVD growth process (Wen et al. 2001). The crystallinity of Ag nanocrystals on the CNTs is confirmed by lattice fringes indexed in the HRTEM image of Fig. 13(b). The measured lattice spacings of 0.20 and 0.23 nm correspond to the (200) and (111) planes of silver crystal, respectively.

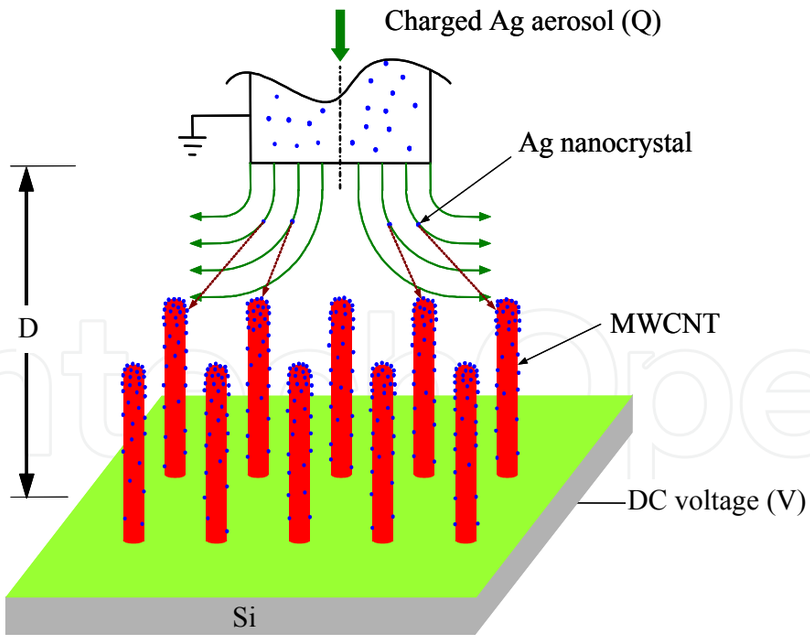


Fig. 11. Schematic diagram for the assembly of Ag nanocrystals onto vertically aligned MWCNTs. Reprinted with permission from (Lu et al. 2007). Copyright 2007 ACS

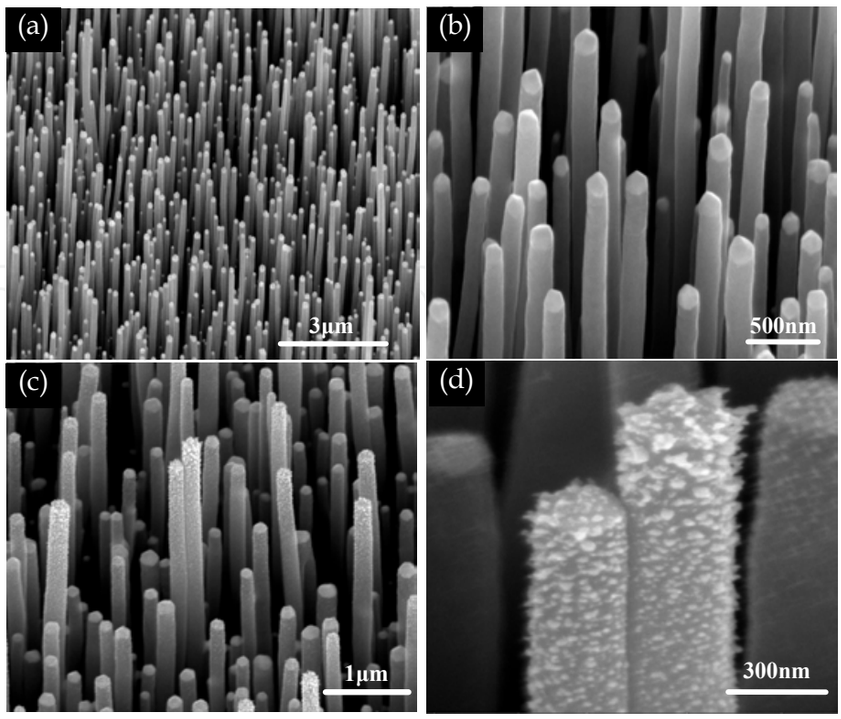


Fig. 12. SEM images of as-grown MWCNT array on a silicon substrate at (a) lower magnification and (b) higher magnification; (c) evidence of NPs coating MWCNTs at a lower magnification and (d) a higher magnification image of a region in image (c), showing NPs deposited on the external surfaces and tips of the MWCNTs. Reprinted with permission from (Lu et al. 2007). Copyright 2007 ACS

The electric field and flow residence time are two critical parameters that govern the nanocrystal assembly process. In this study, the gas flow rate (total flow residence time) was fixed and it is thought that the electric field distribution determines the final Ag NP distribution on the CNTs. There are varying CNT heights in the array shown in Fig. 12, and more NPs are distributed at the tip of taller CNTs, which is likely due to a larger field enhancement for these taller CNTs, and perhaps also due in part to shadowing effects. The CNTs in the array are close to each other and the proximity effect (field screening effect) results in field enhancement only at the tip portion of the CNTs and a larger field enhancement is expected at the tips of taller CNTs. The higher electric field can attract larger NPs with smaller electrical mobilities (for the same charge level on all NPs). The observed larger NPs near the tip of CNTs suggest the critical role of the electric field on the assembly process, since shadowing effects alone should not lead to the variation in NP size along the CNT length.
A similar variation in NP areal density and size has been observed on isolated CNTs. Figure 14(a) shows an SEM image of an isolated CNT coated with Ag NPs from the tip to the root, and with the upper portion of the tube enlarged in Fig. 14(b). Both the NP areal density and the average NP size decrease along the CNT from the tip to its root. For an isolated CNT, the proximity and shadowing effects are not present, and a variation of the NP distribution along the full tube length can only be attributed to the variation in the electric field along the tube axis. Therefore, the results clearly support the critical role of the electric field during the assembly process.

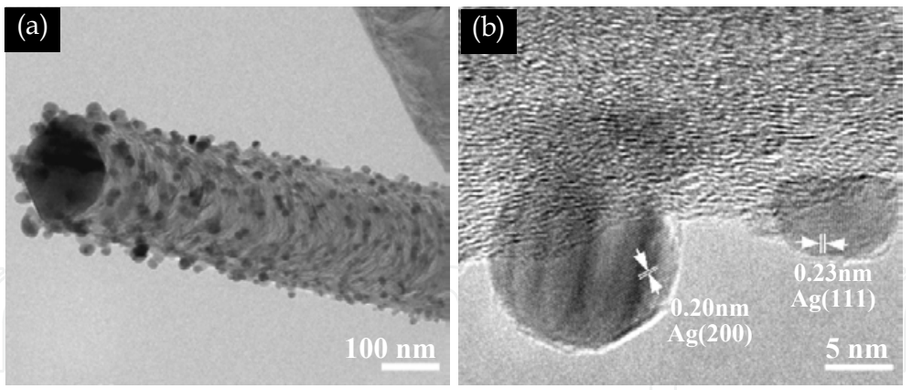


Fig. 13. (a) TEM image of a nanocrystal-coated MWCNT scratched from the Si wafer. (b) HRTEM image showing lattice fringes of Ag nanocrystals deposited on a MWCNT. Reprinted with permission from (Lu et al. 2007). Copyright 2007 ACS

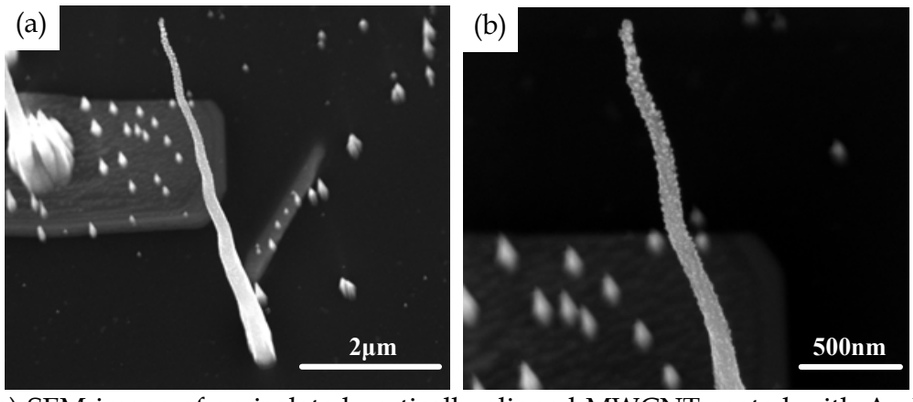


Fig. 14. (a) SEM image of an isolated vertically-aligned MWCNT coated with Ag NPs, and (b) the enlarged view of (a) showing variations of the NP size and areal density along the length of the CNT. Reprinted with permission from (Lu et al. 2007). Copyright 2007 ACS

### 3.5 Modeling of electric field enhancement along CNTs for two cases

The electric field distribution near the CNT surface was modeled in an attempt to understand the experimental observations. The vertical CNT was modeled as a cylinder with a hemispherical cap (Read & Bowring 2004; Podenok et al. 2006). To simplify the model, a 2-D computational domain with vertical CNT(s) against a flat plane is considered. The CNT is assumed to have the same dimensions as those used in experiments, i.e., 150 nm in diameter and 10 μm in length. The electric field distribution over the domain is computed by numerically solving the Laplace equation using "charged particle optics software" (CPO version 5.2, CPO Ltd., 2004). The field enhancement factor ($\gamma$), which is defined as the ratio of the local field to that of the uniform field that would exist between two smooth plates without the CNT(s) present, was obtained along the length of the CNT and is discussed further below.

The electric field distribution was calculated for a single isolated CNT and for a four-tube square array with the same inter-tube spacing (500 nm) as that of the experimental sample. Figure 15 shows that in both cases $\gamma$ increases monotonically from the root to the tip of the CNT. The field enhancement is much weaker for the four-tube array than for the isolated

CNT due to the shielding effect, as expected. The modeling results are comparable with those published in the literature (Read & Bowring 2004; Podenok et al. 2006). Such modeling points to the possible influence of field enhancement on where nanocrystals are deposited during the ESFDA process.

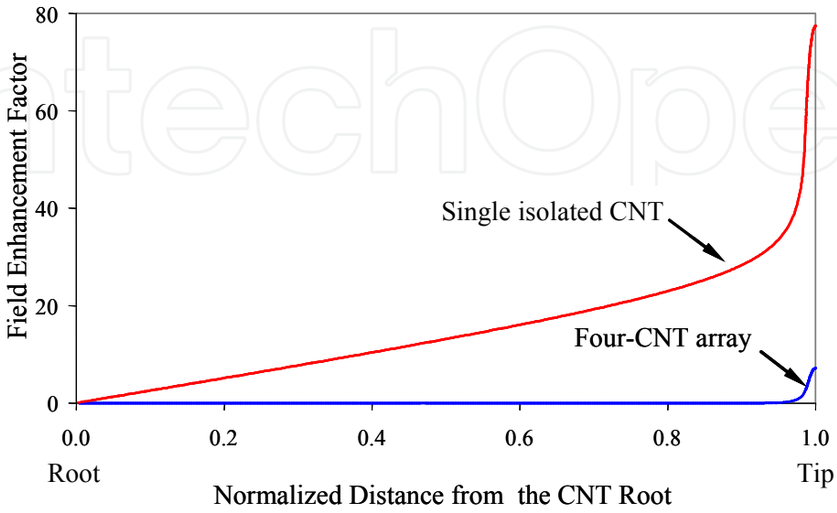


Fig. 15. The electric field enhancement factor along the length of the CNT for a single isolated, vertically-aligned CNT, and a four-tube square array with inter-tube spacing of 500 nm. The CNTs are 10 μm in length and 150 nm in diameter. The spacing between the CNT substrate and the counter electrode is 2 mm. Reprinted with permission from (Lu et al. 2007). Copyright 2007 ACS

### 3.6 Assembling colloidal NPs onto CNTs

Aerosol synthesis methods could be limited in producing NPs in terms of material type and control in the nanocrystal properties, and such methods typically produce NPs with a relatively broad size distribution (Fissan et al. 2003). Colloidal synthesis, on the other hand, affords considerable control over particle size and structure since the surface chemistry can be manipulated by adjusting the solution properties (Murray et al. 1993). Combining with aerosolization techniques, e.g., electrospray (Lenggoro et al. 2002), NPs in aqueous suspension can be deposited onto CNTs as well using the ESFDA technique (Mao et al. 2008).

Figure 16(a) is a schematic of the system that comprises both the electrospray process and the ESFDA process. The conductive colloidal suspension applied with a high dc voltage is extracted through a capillary submerged in the suspension due to the capillary effect and the capillary inlet/outlet pressure difference. The liquid ejected from the capillary is atomized to form charged fine droplets due to the electrohydrodynamic break-up. Then, a fraction of the aerosolized colloidal NPs is deposited on CNTs via the ESFDA process. The assembly time is typically on the order of hours and is dependent on the colloid concentration and the desired areal density of nanocrystals on CNTs.

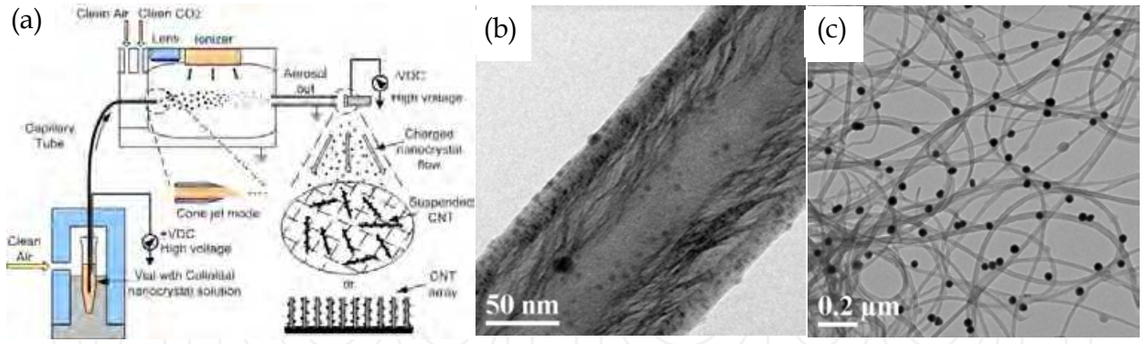


Fig. 16. (a) Schematic of the nanocrystal aerosolization by an electrospray process and the subsequent assembly of nanocrystals onto random CNTs or vertically-aligned CNTs by ESFDA. (b) and (c) TEM images of CNT(s) coated with 3 nm CdSe nanocrystals and 40 nm Au nanocrystals, respectively. Reprinted with permission from (Mao et al. 2008). Copyright 2008 IOP

Figures 16(b) is a TEM image of a single CNT scratched from a vertically-aligned CNT array coated with CdSe nanocrystals. The CdSe nanocrystals (small black dots) are distributed uniformly on the external surface of the CNT. The CdSe colloidal suspension with size-selected nanocrystals was produced by a one-pot synthesis method and the reaction temperature was accurately controlled to achieve the desired CdSe nanocrystal size (Robel et al. 2007). Figure 16(c) shows a TEM image of CNTs (20-40 nm in diameter) coated with 40 nm Au NPs. Colloidal suspensions with 40 nm Au nanocrystals in $H_2O$ were purchased from BB International (stock #10136).

## 4. Interaction between CNTs and NPs

Understanding the binding mechanism between CNTs and NPs will assist the rational design and use of these novel CNT-NP hybrid structures. Attaching NPs onto CNTs can be achieved through covalent, noncovalent, or electrostatic interactions, which can influence the properties and potential applications of the CNT-NP hybrid structures. Covalent bonding between the nanocrystal and the CNT was obtained through different acid treatments to create such linking groups as carboxyl (-COOH), carbonyl (-C=O), and hydroxyl (-OH); however, the mechanical and particularly the electronic transport properties of the CNT may degrade significantly after acid treatment due to the introduction of defects (Zamudio et al. 2006). The noncovalent attachment of nanocrystals is more likely to preserve the unique properties of low-defect CNTs.

Since the ESFDA assembly is performed at room temperature in inert gas, the chance of noncovalent binding between NP and nanotube is enhanced. The behavior of the CNT-NP structure at higher-than-ambient temperatures in air is also relevant for many applications. For example, metal oxide gas sensors are typically operated at elevated temperatures (200-500°C) to maximize their sensitivity (Shimizu & Egashira 1999); therefore, it is useful to understand how particle distribution, binding, and morphology, are influenced by heating in air, following creation of the hybrid structures by the aforementioned aerosol deposition at room temperature and under inert gas. Thus, following the creation of the CNT-NP hybrid structures by the ESFDA process at room temperature and under inert gas, it is

useful to investigate how particle distribution, binding, and morphology are influenced by heating in air and reveal the possible interaction between the NP and CNT.

The evolution of the hybrid structure was studied using TEM imaging after particular heating cycles were applied in air (Zhu et al. 2007). Regions on the TEM grid were identified and imaged prior to heating. The location of each region was determined by its position with respect to the central mark of the grid for a given grid orientation. After the target regions were selected, the TEM grid containing the Ag NP-CNT hybrid structures were placed into an oven with a preset temperature and held for one hour (h) at that temperature. At the end of each heating cycle, the sample was removed from the oven, quickly cooled to room temperature, and immediately imaged with the TEM. The first of the three heating cycles was performed with a preset oven temperature of 100°C, the second at 200°C, and the third at 300°C. The same sample was used for each cycle.

Figure 17(a) is a TEM image of the original sample of CNTs covered with Ag. Figure 17(b) shows the TEM image of the same Ag NP-CNT sample after being heated in air at 100, 200, and 300°C for 1 h each. Ripening evidently occurred during the heating as smaller Ag NPs move and merge with larger Ag NPs. As a result, the areal density of Ag NPs on the CNT decreases while the average diameter of Ag NPs increases.

Smaller NPs on the CNT surface may be energetically less stable than larger ones due to their relatively larger surface-to-volume ratio. As a result, the transformation of smaller particles into larger ones could be energetically favorable on the CNT surface. In addition, smaller NPs are likely to diffuse more readily than larger ones; thus, the growth of the larger particles could simply be a consequence of the smaller ones moving and colliding with the larger particles to form even larger particles. Coalescence of the merged larger particles can also be inferred based on the TEM image, as the observed particles are nearly spherical, as shown in Fig. 17(b). Although the vapor pressure of Ag NPs is known to be higher than that of bulk Ag (Blackman et al. 1968), at these relatively low temperatures and for the total exposure time of 3 h, it is unlikely that a significant fraction of Ag is lost (if any) by atomic evaporation.

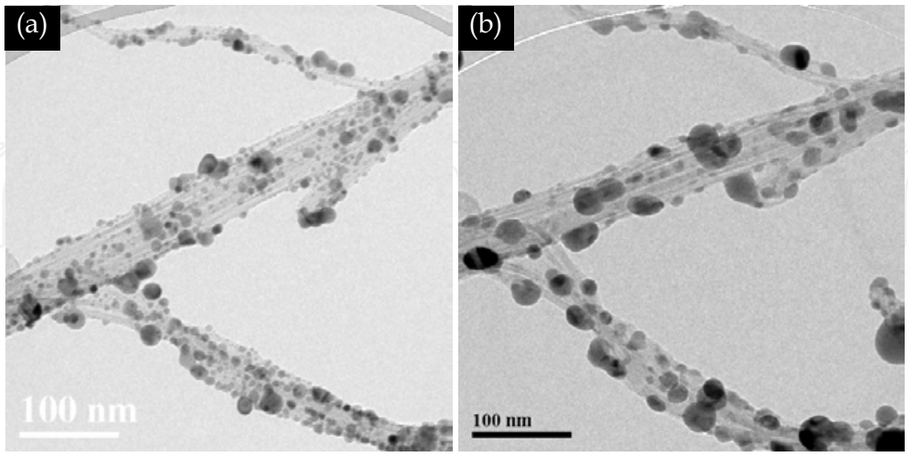


Fig. 17. TEM images of (a) the original Ag NP-CNT structure and (b) the Ag NP-CNT structure after being successively heated at 100, 200, and 300°C for 1 hr each.

The ripening of Ag NPs on CNTs can be anticipated from the studies of Ag clusters/particles located on other surfaces (Rosenfeld et al. 1998; Morgenstern et al. 1999; Meyer et al. 2007) or embedded in polymer films (Heilmann & Werner 1998). Two possible mechanisms are known to be responsible for the ripening process, namely Ostwald ripening and particle migration and coalescence (Wynblatt & Gjostein 1975; Wynblatt & Gjostein 1976). In an Ostwald ripening process, atomic species from smaller particles transport to larger particles either by surface diffusion along the substrate or by vapor phase diffusion due to the difference in the chemical potentials between smaller and larger particles. Under the particle migration and coalescence mechanism, smaller particles migrate on the substrate surface and then collide/coalesce with larger particles.

Although it is difficult to obtain a detailed mechanistic insight based solely on the change in particle size distribution before and after heating (Datye et al. 2006), additional comparison of successive TEM images has allowed us to infer the occurrence of Ag particle migration and coalescence in our experiments. Of course, we cannot exclude the possibility of Ostwald ripening, and observation using an in situ heating experiment inside a TEM chamber might further elucidate the mechanism (Liu et al. 2004). There is the possibility of competition between possible thermodesorption of the whole Ag NP from the CNT surface versus migration of the NP on the CNT surface; the rates for both are expected to increase with increasing temperature. The TEM images obtained after the three 1 h thermal treatments at 100, 200, and 300°C show that surface migration of Ag particles occurs more readily than thermodesorption of Ag NPs, even at 300°C. The more-ready surface migration thus leads to the ripening of the Ag NPs.

The migration of Ag NPs at these relatively low temperatures suggests a weak interaction between Ag NPs and CNTs. It is well known that some transition elements chemically bond to carbon (Zhang et al. 2000). This is attributed to the distribution of d electrons in such transition elements. Since Ag atoms have no d vacancy orbitals, they have a very weak affinity for bonding with carbon atoms (Durgun et al. 2003). As a result, Ag NPs most likely attach to CNTs through van der Waals forces instead of chemical bonds (Zhang & Dai 2000). Because the CNT surface is relatively smooth, we speculate that the barrier for thermally activated migration of Ag NPs is low and thus favors surface migration and ripening.

## 5. Gas-Sensing Platform Based on the CNT-NP Structure

SWCNTs have been used to detect gaseous species such as $NO_2$ and $NH_3$ at room temperature due to the variation in the electrical resistance of CNTs upon exposure to these gases (Kong et al. 2000). The sensing response is attributed to the *p*-type conductivity of semiconducting CNTs and the electrical charge transfer between CNTs and gaseous molecules. Bare CNTs are insensitive to some gaseous molecules such as CO and $H_2$ (Kong et al. 2001); in the case of $H_2$, it was found that the binding energy between a $H_2$ molecule and the outer surface of a bare CNT is so weak that the physisorption bond can easily break (Dag et al. 2005). CNT surface functionalization, e.g., with Pd nanoparticles (Kong et al. 2001) and Pt nanoparticles (Kumar & Ramaprabhu 2006), has been exploited to extend the spectrum of gases that CNT-based sensors can detect. Rutile tin oxide ($SnO_2$) is an *n*-type semiconducting material widely used in gas sensing applications (McAleer et al. 1987). The existing $SnO_2$ sensors typically operate at temperatures over 200 °C (Gopel 1996) to enhance the surface adsorption/reaction kinetics and sensitivity, which require continuous heating

of the sensor and increase the sensor cost. The high-temperature operation is also undesirable in many situations, particularly in an explosive environment because high temperatures could trigger an explosion.

We have investigated the feasibility of developing a gas-sensing platform based on hybrid nanostructures consisting of discrete $SnO_2$ NPs uniformly distributed on the surface of MWCNTs (Fig. 18). The hybrid nanostructures were synthesized (Fig. 19a) by the ESFAD process, which assembled aerosol $SnO_2$ nanocrystals onto MWCNTs pre-deposited on e-beam lithographically patterned Au interdigitated electrodes. Figure 19(b) is an SEM image of the sensing device after the $SnO_2$ NP assembly by the ESFDA. The MWCNTs bridging a pair of neighboring electrode fingers clearly show $SnO_2$ nanocrystals decorated on their external surfaces.

Through the marriage between CNTs and $SnO_2$ NPs, the hybrid $SnO_2$ NP-CNT structure exhibits high sensitivity to low-concentration gases ($NO_2$, $H_2$, and CO) at room temperature. The dynamic response of the $SnO_2$ nanocrystal-MWCNT sensor for detecting 100 ppm $NO_2$ is shown in Fig. 19(c). The sensor was operated at room temperature and periodically exposed to clean air flow (2 lpm) for 10 minutes (min) to record a base value of the sensor conductance; 100 ppm $NO_2$ diluted in air (2 lpm) for 10 min to register a sensing signal; and clean air flow (2 lpm) again for 20 min to recover the device. Five such cycles were repeated, as shown in Fig. 19(c), and the sensing behavior appeared fairly reproducible. The sensor sensitivity, which is evaluated as the ratio of $(G_g\text{-}G_a)/G_a$, where $G_a$ is the sensor conductance in air and $G_g$ is that in the challenging gas, was ~ 1.8. The same $SnO_2$-CNT sensor also exhibited sensitivity to $H_2$ and CO, although bare CNTs are insensitive to these gaseous molecules. Figure 19(d) shows the room-temperature sensing performance of the $SnO_2$ nanocrystal-MWCNT sensor for detecting 1% and 1000 ppm $H_2$ and 100 ppm CO diluted in air. For CO, the sensitivity was ~ 0.11; for 1% $H_2$, the average sensitivity was ~ 0.17; and for 1000 ppm $H_2$, the average sensitivity was ~ 0.10. The $H_2$ sensing performance is comparable with those reported in the literature for CNTs functionalized with Pd (Kong et al. 2001) or Pt (Kumar & Ramaprabhu 2006) nanoparticles.

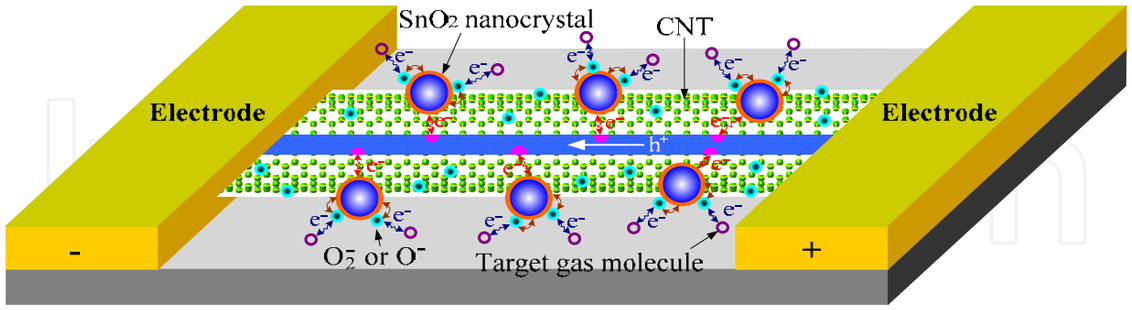


Fig. 18. Discrete $SnO_2$ nanocrystals supported on an individual CNT as a new gas-sensing platform. The modulation of the CNT electrical transport property through the interaction between the $SnO_2$ NP and the surrounding environment is harnessed for gas-sensing. Reprinted with permission from (Lu et al. 2009). Copyright 2009 WILEY

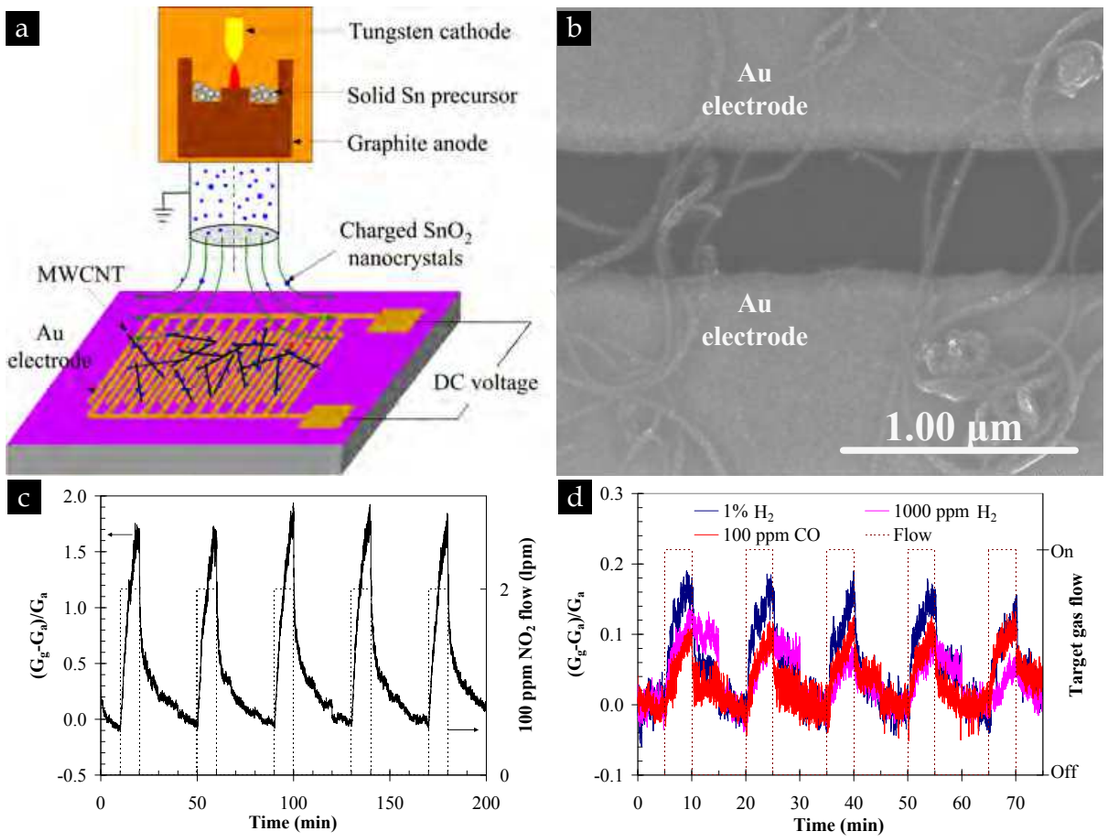


Fig. 19. (a) Assembly of charged $SnO_2$ NPs onto MWCNTs dispersed on an Au interdigitated electrode using ESFDA. (b) A section of the sensor after assembly of $SnO_2$ NPs onto MWCNTs. Dynamic response of the $SnO_2$ NP-MWCNT sensor for detecting room-temperature (c) 100 ppm $NO_2$ and (d) 1% and 1000 ppm $H_2$, and 100 ppm CO diluted in air. Reprinted with permission from (Lu et al. 2009). Copyright 2009 WILEY

The hybrid platform provides a radically new opportunity to engineer sensing devices with quantum-mechanical attributes by taking advantage of the electronic transfer between the nanocrystal and the CNT. The hybrid system as a sensing element is potentially superior to either of the constituent components. CNTs coated with discrete $SnO_2$ NPs can detect gases that are normally undetectable by bare CNTs. Attaching NPs onto CNTs leads to more active sites for the adsorption of gaseous molecules and thus a higher sensitivity than bare CNTs. The operating temperature for the hybrid sensing platform can be as low as room temperature, in contrast to the required high temperature (typically above 200 °C) for $SnO_2$ sensors. Moreover, the differential sensitivity between CNTs and $SnO_2$ NPs, the spacing between $SnO_2$ NPs (areal density of $SnO_2$ NPs on CNTs), and doping of $SnO_2$ NPs offer tremendous flexibility in adjusting the sensitivity of individual sensors, which can be conveniently used to engineer the selectivity of gas sensors.

## 6. Summary and Outlook

Our research on CNT-NP hybrid structures began as a scientific curiosity. It has advanced to a stage where the methods to produce these hybrid nanostructures are available, and much more attention has been paid to such materials because of their potential widespread applications in many areas.

The ESFDA technique can be used to efficiently coat randomly dispersed and vertically-aligned CNTs with various aerosol NPs. An intrinsic NP size selection has been observed during the assembly process. The final NP size distribution and areal density can be controlled through flow residence time/electric field or assembly time, respectively. For vertically-aligned CNTs, the electric field distribution near the CNT surface was computed using a simple model of the CNT as a cylinder with a hemispherical cap; the field enhancement factor increases from the root to the tip of the CNT for the two cases studied. The areal density and size distributions of nanocrystals observed along the CNTs in the vertical array can be rationalized by the variation of the electric field near the CNT surface; however, it is possible that shadowing effects also play a minor role on the variation in the nanocrystal areal density, but not on the nanocrystal size.

NP production is not limited to the mini-arc reactor used in our earlier study. NPs produced by other aerosol reactors or by aerosolization of colloidal NPs can also be used for the assembly, although an additional charging device may be needed in some cases. Due to the material independence of electrostatic force, the capability of ESFDA has been greatly expanded. One can imagine that NPs of multiple materials, particularly interweaving metal and semiconductor/magnetic nanocrystals, can be assembled onto CNTs. These interesting multicomponent structures will open up new opportunities in several interdisciplinary fields.

While the controlled production of the hybrid nanostructures is being perfected, a pressing area of research is to understand the synergistic interaction between the two nanocomponents, i.e., NPs and CNTs. Equally important is the understanding of the properties of hybrid nanostructures, which can be tailored for various innovative applications.

## Acknowledgements

This work was financially supported by the National Science Foundation, the University of Wisconsin-Milwaukee (UWM), the UWM Research Foundation, and Science & Technology Committee of Shanghai, China. The authors would like to thank collaborators R. S. Ruoff, Z. F. Ren, M. Gajdardziska-Josifovska, and L. E. Ocola. The electrodes of sensing devices were fabricated at the Center for Nanoscale Materials at Argonne National Laboratory.

## 7. References

Alivisatos, A. P. (1996). Semiconductor clusters, nanocrystals, and quantum dots, *Science*, **271,** 5251, pp. 933-937.

Anson, A.; Lafuente, E.; Urriolabeitia, E.; Navarro, R.; Benito, A. M.; Maser, W. K. & Martinez, M. T. (2006). Hydrogen capacity of palladium-loaded carbon materials, *J. Phys. Chem. B*, **110,** 13, pp. 6643-6648.

Berber, S.; Kwon, Y. K. & Tomanek, D. (2000). Unusually high thermal conductivity of carbon nanotubes, *Phys. Rev. Lett.*, **84,** 20, pp. 4613-4616.

Blackman, M.; Lisgarten, N. D. & Skinner, L. M. (1968). Surface Energy and Evaporation Rate of Spherical Particles of Radii less than 500 [angst], *Nature*, **217,** 5135, pp. 1245-1246.

Chen, J. H. & Davidson, J. H. (2003). Model of the negative DC corona plasma: comparison to the positive DC corona plasma, *Plasma Chem. Plasma Process.*, **23,** 1, pp. 83-102.

Chen, J. H. & Lu, G. H. (2006). Controlled decoration of carbon nanotubes with nanoparticles, *Nanotechnol.*, **17,** 12, pp. 2891-2894.

Chen, J. H.; Lu, G. H.; Zhu, L. Y. & Flagan, R. C. (2007). A simple and versatile mini-arc plasma source for rapid nanocrystal synthesis, *J. Nanopart. Res.*, **9,** 2, pp. 203-213.

Conner, W. C. & Falconer, J. L. (1995). Spillover in Heterogeneous Catalysis, *Chem. Rev.*, **95,** 3, pp. 759-788.

Dag, S.; Ozturk, Y.; Ciraci, S. & Yildirim, T. (2005). Adsorption and dissociation of hydrogen molecules on bare and functionalized carbon nanotubes, *Phys. Rev. B*, **72,** 15, pp. 155404.

Datye, A. K.; Xu, Q.; Kharas, K. C. & McCarty, J. M. (2006). Particle size distributions in heterogeneous catalysts: What do they tell us about the sintering mechanism?, *Catal. Today*, **111,** 1-2, pp. 59-67.

de Heer, W. A. (2004). Nanotubes and the Pursuit of Applications, *Mater. Res. Soc. Bull.*, **29,** 4, pp. 281-285.

Dresselhaus, M. S.; Dresselhaus, G. & Avouris, P., Eds. (2001). *Carbon nanotubes: synthesis, structure, properties and applications*, Springer-Verlag, Berlin.

Dresselhaus, M. S. a. D., H. (2004). Carbon Nanotubes: Continued Innovations and Challenges, *Mater. Res. Soc. Bull.*, **29,** 4, pp. 237-239.

Durgun, E.; Dag, S.; Bagci, V. M. K.; Gulseren, O.; Yildirim, T. & Ciraci, S. (2003). Systematic study of adsorption of single atoms on a carbon nanotube, *Phys. Rev. B, 67, 20, pp. 201401.*

Fissan, H.; Kennedy, M. K.; Krinke, T. J. & Kruis, F. E. (2003). Nanoparticles from the gas phase as building blocks for electrical devices, *J. Nanopart. Res.*, **5,** 3-4, pp. 299-310.

Georgakilas, V.; Gournis, D.; Tzitzios, V.; Pasquato, L.; Guldi, D. M. & Prato, M. (2007). Decorating carbon nanotubes with metal or semiconductor nanoparticles, *J. Mater. Chem.*, **17,** 26, pp. 2679-2694.

Gopel, W. (1996). Ultimate limits in the miniaturization of chemical sensors, *Sensors and Actuators a-Physical*, **56,** 1-2, pp. 83-102.

Guldi, D. M.; Rahman, G. M. A.; Sgobba, V.; Kotov, N. A.; Bonifazi, D. & Prato, M. (2006). CNT-CdTe versatile donor-acceptor nanohybrids, *J. Am. Chem. Soc.*, **128,** 7, pp. 2315-2323.

Heilmann, A. & Werner, J. (1998). In situ observation of microstructural changes of embedded silver particles, *Thin Solid Films*, **317,** 1-2, pp. 21-26.

Hinds, B. J.; Chopra, N.; Rantell, T.; Andrews, R.; Gavalas, V. & Bachas, L. G. (2004). Aligned multiwalled carbon nanotube membranes, *Science*, **303,** 5654, pp. 62-65.

Huang, Z. P.; Wu, J. W.; Ren, Z. F.; Wang, J. H.; Siegal, M. P. & Provencio, P. N. (1998). Growth of highly oriented carbon nanotubes by plasma-enhanced hot filament chemical vapor deposition, *Appl. Phys. Lett.*, **73,** 26, pp. 3845-3847.

Iijima, S. (1991). Helical Microtubules of Graphitic Carbon, *Nature*, **354,** 6348, pp. 56-58.

Iijima, S. & Ichihashi, T. (1993). Single-Shell Carbon Nanotubes of 1-nm Diameter, *Nature*, **363,** 6430, pp. 603-605.

Jung, Y. J.; Kar, S.; Talapatra, S.; Soldano, C.; Viswanathan, G.; Li, X. S.; Yao, Z. L.; Ou, F. S.; Avadhanula, A.; Vajtai, R.; Curran, S.; Nalamasu, O. & Ajayan, P. M. (2006). Aligned carbon nanotube-polymer hybrid architectures for diverse flexible electronic applications, *Nano Lett.*, **6,** 3, pp. 413-418.

Kang, S. J.; Kocabas, C.; Ozel, T.; Shim, M.; Pimparkar, N.; Alam, M. A.; Rotkin, S. V. & Rogers, J. A. (2007). High-performance electronics using dense, perfectly aligned arrays of single-walled carbon nanotubes, *Nat. Nanotechnol.*, **2,** 4, pp. 230-236.

Khoo, K. H. & Chelikowsky, J. R. (2009). Electron transport across carbon nanotube junctions decorated with Au nanoparticles: Density functional calculations, *Phys. Rev. B*, **79,** 20, pp. 205422.

Kim, B. & Sigmund, W. M. (2004). Functionalized multiwall carbon nanotube/gold nanoparticle composites, *Langmuir*, **20,** 19, pp. 8239-8242.

Kim, Y. A.; Muramatsu, H.; Hayashi, T.; Endo, M.; Terrones, M. & Dresselhaus, M. S. (2004). Thermal stability and structural changes of double-walled carbon nanotubes by heat treatment, *Chem. Phys. Lett.*, **398,** 1-3, pp. 87-92.

Kong, B. S.; Jung, D. H.; Oh, S. K.; Han, C. S. & Jung, H. T. (2007). Single-walled carbon nanotube gold nanohybrids: Application in highly effective transparent and conductive films, *J. Phys. Chem. C*, **111,** 23, pp. 8377-8382.

Kong, J.; Chapline, M. G. & Dai, H. J. (2001). Functionalized carbon nanotubes for molecular hydrogen sensors, *Adv. Mater.*, **13,** 18, pp. 1384-1386.

Kong, J.; Franklin, N. R.; Zhou, C. W.; Chapline, M. G.; Peng, S.; Cho, K. J. & Dai, H. J. (2000). Nanotube molecular wires as chemical sensors, *Science*, **287,** 5453, pp. 622-625.

Kongkanand, A.; Dominguez, R. M. & Kamat, P. V. (2007). Single wall carbon nanotube scaffolds for photoelectrochemical solar cells. Capture and transport of photogenerated electrons, *Nano Lett.*, **7,** 3, pp. 676-680.

Kongkanand, A.; Vinodgopal, K.; Kuwabata, S. & Kamat, P. V. (2006). Highly dispersed Pt catalysts on single-walled carbon nanotubes and their role in methanol oxidation, *J. Phys. Chem. B*, **110,** 33, pp. 16185-16188.

Kumar, M. K. & Ramaprabhu, S. (2006). Nanostructured Pt functionlized multiwalled carbon nanotube based hydrogen sensor, *J. Phys. Chem. B*, **110,** 23, pp. 11291-11298.

Landi, B. J.; Castro, S. L.; Ruf, H. J.; Evans, C. M.; Bailey, S. G. & Raffaelle, R. P. (2005). CdSe quantum dot-single wall carbon nanotube complexes for polymeric solar cells, *Sol. Energy Mater. Sol. Cells*, **87,** 1-4, pp. 733-746.

Lee, H.; Yoon, S. W.; Kim, E. J. & Park, J. (2007). In-situ growth of copper sulfide nanocrystals on multiwalled carbon nanotubes and their application as novel solar cell and amperometric glucose sensor materials, *Nano Lett.*, **7,** 3, pp. 778-784.

Lenggoro, I. W.; Xia, B.; Okuyama, K. & de la Mora, J. F. (2002). Sizing of colloidal nanoparticles by electrospray and differential mobility analyzer methods, *Langmuir*, **18,** 12, pp. 4584-4591.

Li, L. Y.; Yang, Y.; Yang, G. L.; Chen, X. M.; Hsiao, B. S.; Chu, B.; Spanier, J. E. & Li, C. Y. (2006). Patterning polyethylene oligomers on carbon nanotubes using physical vapor deposition, *Nano Lett.*, **6,** 5, pp. 1007-1012.

Liu, H.; Kozlov, A. I.; Kozlova, A. P.; Shido, T.; Asakura, K. & Iwasawa, Y. (1999). Active oxygen species and mechanism for low-temperature CO oxidation reaction on a TiO2-supported Au catalyst prepared from Au(PPh3)(NO3) and As-precipitated titanium hydroxide, *J. Catal.*, **185,** 2, pp. 252-264.

Liu, J.; Casavant, M. J.; Cox, M.; Walters, D. A.; Boul, P.; Lu, W.; Rimberg, A. J.; Smith, K. A.; Colbert, D. T. & Smalley, R. E. (1999). Controlled deposition of individual single-walled carbon nanotubes on chemically functionalized templates, *Chem. Phys. Lett.*, **303,** 1-2, pp. 125-129.

Liu, R. J.; Crozier, P. A.; Smith, C. M.; Hucul, D. A.; Blackson, J. & Salaita, G. (2004). In situ electron microscopy studies of the sintering of palladium nanoparticles on alumina during catalyst regeneration processes, *Microsc. Microanal.*, **10,** 1, pp. 77-85.

Lu, G. H.; Ocola, L. E. & Chen, J. H. (2009). Room-Temperature Gas Sensing Based on Electron Transfer between Discrete Tin Oxide Nanocrystals and Multiwalled Carbon Nanotubes, *Adv. Mater.*, **21,** 24, pp. 2487-2491.

Lu, G. H.; Zhu, L. Y.; Wang, P. X.; Chen, J. H.; Dikin, D. A.; Ruoff, R. S.; Yu, Y. & Ren, Z. F. (2007). Electrostatic-force-directed assembly of ag nanocrystals onto vertically aligned carbon nanotubes, *J. Phys. Chem. C*, **111,** 48, pp. 17919-17922.

Mao, S.; Lu, G. H. & Chen, J. H. (2008). Coating carbon nanotubes with colloidal nanocrystals by combining an electrospray technique with directed assembly using an electrostatic field, *Nanotechnol.*, **19,** 45, pp. 455610.

McAleer, J. F.; Moseley, P. T.; Norris, J. O. W. & Williams, D. E. (1987). Tin Dioxide Gas Sensors .1. Aspects of the Surface-Chemistry Revealed by Electrical Conductance Variations, *Journal of the Chemical Society-Faraday Transactions I*, **83**, pp. 1323-1346.

Meyer, R.; Ge, Q. F.; Lockemeyer, J.; Yeates, R.; Lemanski, M.; Reinalda, D. & Neurock, M. (2007). An ab initio analysis of adsorption and diffusion of silver atoms on alumina surfaces, *Surf. Sci.*, **601,** 1, pp. 134-145.

Morgenstern, K.; Rosenfeld, G. & Comsa, G. (1999). Local correlation during Ostwald ripening of two-dimensional islands on Ag(111), *Surf. Sci.*, **441,** 2-3, pp. 289-300.

Mu, Y. Y.; Liang, H. P.; Hu, J. S.; Jiang, L. & Wan, L. J. (2005). Controllable Pt nanoparticle deposition on carbon nanotubes as an anode catalyst for direct methanol fuel cells, *J. Phys. Chem. B*, **109,** 47, pp. 22212-22216.

Murray, C. B.; Norris, D. J. & Bawendi, M. G. (1993). Synthesis and characterization of nearly monodisperse CdE (E = sulfur, selenium, tellurium) semiconductor nanocrystallites, *J. Am. Chem. Soc.*, **115,** 19, pp. 8706-8715.

Peng, X. H.; Chen, J. Y.; Misewich, J. A. & Wong, S. S. (2009). Carbon nanotube-nanocrystal heterostructures, *Chem. Soc. Rev.*, **38,** 4, pp. 1076-1098.

Podenok, S.; Sveningsson, M.; Hansen, k. & Campbell, E. E. B. (2006). Electric Field Enhancement Factors aound a Metallic, End-Capped Cylinder, *Nano*, **1,** 1, pp. 87-93.

Read, F. H. & Bowring, N. J. (2004). Field enhancement factors of one-dimensional and two-dimensional arrays of nanotubes, *Microelectron. Eng.*, **73-74**, pp. 679-685.

Robel, I.; Bunker, B. A. & Kamat, P. V. (2005). Single-walled carbon nanotube-CdS nanocomposites as light-harvesting assemblies: Photoinduced charge-transfer interactions, *Adv. Mater.*, **17,** 20, pp. 2458-2463.

Robel, I.; Girishkumar, G.; Bunker, B. A.; Kamat, P. V. & Vinodgopal, K. (2006). Structural changes and catalytic activity of platinum nanoparticles supported on C-60 and carbon nanotube films during the operation of direct methanol fuel cells, *Appl. Phys. Lett.*, **88,** 7, pp. 073113.

Robel, I.; Kuno, M. & Kamat, P. V. (2007). Size-dependent electron injection from excited CdSe quantum dots into TiO2 nanoparticles, *J. Am. Chem. Soc., 129, 14, pp. 4136-4137.*

Rosenfeld, G.; Morgenstern, K.; Beckmann, I.; Wulfhekel, W.; Laegsgaard, E.; Besenbacher, F. & Comsa, G. (1998). Stability of two-dimensional clusters on crystal surfaces: From Ostwald ripening to single-cluster decay, *Surf. Sci.*, **404,** 1-3, pp. 401-408.

Saito, R., G. Dresselhaus, and M.S. Dresselhaus, (1998). *Physical Properties of Carbon Nanotubes*, Imperial College Press., London.

Scher, E. C.; Manna, L. & Alivisatos, A. P. (2003). Shape control and applications of nanocrystals, *Philosophical Transactions of the Royal Society of London Series a-Mathematical Physical and Engineering Sciences*, **361,** 1803, pp. 241-255.

Seinfeld, J. H. & Pandis, S. N. (1998). *Atmospheric Chemistry and Physics: From Air Pollution to Climate Change*, John Wiley & Sons, Inc., New York.

Shao, Y. Y.; Liu, J.; Wang, Y. & Lin, Y. H. (2009). Novel catalyst support materials for PEM fuel cells: current status and future prospects, *J. Mater. Chem.*, **19,** 1, pp. 46-59.

Shimizu, Y. & Egashira, M. (1999). Basic aspects and challenges of semiconductor gas sensors, *Mrs Bulletin*, **24,** 6, pp. 18-24.

Sun, Y. G. & Wang, H. H. (2007). High-performance, flexible hydrogen sensors that use carbon nanotubes decorated with palladium nanoparticles, *Adv. Mater.*, **19,** 19, pp. 2818-2823.

Treacy, M. M. J.; Ebbesen, T. W. & Gibson, J. M. (1996). Exceptionally high Young's modulus observed for individual carbon nanotubes, *Nature*, **381,** 6584, pp. 678-680.

Valden, M.; Lai, X. & Goodman, D. W. (1998). Onset of catalytic activity of gold clusters on titania with the appearance of nonmetallic properties, *Science*, **281,** 5383, pp. 1647-1650.

Wen, J. G.; Huang, Z. P.; Wang, D. Z.; Chen, J. H.; Yang, S. X.; Ren, Z. F.; Wang, J. H.; Calvet, L. E.; Chen, J.; Klemic, J. F. & Reed, M. A. (2001). Growth and characterization of aligned carbon nanotubes from patterned nickel nanodots and uniform thin films, *J. Mater. Res.*, **16,** 11, pp. 3246-3253.

Wolf, A. & Schuth, F. (2002). A systematic study of the synthesis conditions for the preparation of highly active gold catalysts, *Appl. Catal., A*, **226,** 1-2, pp. 1-13.

Wynblatt, P. & Gjostein, N. A. (1975). Supported metal crystallites, *Prog. Solid State Chem.*, **9**, pp. 21-58.

Wynblatt, P. & Gjostein, N. A. (1976). Particle growth in model supported metal catalysts - I Theory, *Acta Metall. Mater.*, **24,** 12, pp. 1165-1174.

Xing, Y. C. (2004). Synthesis and electrochemical characterization of uniformly-dispersed high loading Pt nanoparticles on sonochemically-treated carbon nanotubes, *J. Phys. Chem. B*, **108,** 50, pp. 19255-19259.

Ye, X. R.; Lin, Y. H.; Wai, C. M.; Talbot, J. B. & Jin, S. H. (2005). Supercritical fluid attachment of palladium nanoparticles on aligned carbon nanotubes, *J. Nanosci. Nanotechnol.*, **5,** 6, pp. 964-969.

Yildirim, T. & Ciraci, S. (2005). Titanium-decorated carbon nanotubes as a potential high-capacity hydrogen storage medium, *Phys. Rev. Lett.*, **94,** 17, pp. 175501.

Yu, M. F.; Lourie, O.; Dyer, M. J.; Moloni, K.; Kelly, T. F. & Ruoff, R. S. (2000). Strength and breaking mechanism of multiwalled carbon nanotubes under tensile load, *Science*, **287,** 5453, pp. 637-640.

Zamudio, A.; Elias, A. L.; Rodriguez-Manzo, J. A.; Lope-Urias, F.; Rodriguez-Gattorno, G.; Lupo, F.; Ruhle, M.; Smith, D. J.; Terrones, H.; Diaz, D. & Terrones, M. (2006). Efficient anchoring of silver nanoparticles on N-doped carbon nanotubes, *Small*, **2,** 3, pp. 346-350.

Zamudio, A.; Elias, A. L.; Rodriguez-Manzo, J. A.; Lopez-Urias, F.; Rodriguez-Gattorno, G.; Lupo, F.; Ruhle, M.; Smith, D. J.; Terrones, H.; Diaz, D. & Terrones, M. (2006). Efficient anchoring of silver nanoparticles on N-doped carbon nanotubes, *Small*, **2,** 3, pp. 346-350.

Zhang, Y. & Dai, H. J. (2000). Formation of metal nanowires on suspended single-walled carbon nanotubes, *Appl. Phys. Lett.*, **77,** 19, pp. 3015-3017.

Zhang, Y.; Franklin, N. W.; Chen, R. J. & Dai, H. J. (2000). Metal coating on suspended carbon nanotubes and its implication to metal-tube interaction, *Chem. Phys. Lett.*, **331,** 1, pp. 35-41.

Zhang, Y.; Zhang, X. G.; Zhang, H. L.; Zhao, Z. G.; Li, F.; Liu, C. & Cheng, H. M. (2006). Composite anode material of silicon/graphite/carbon nanotubes for Li-ion batteries, *Electrochim. Acta*, **51,** 23, pp. 4994-5000.

Zheng, L. X.; O'Connell, M. J.; Doorn, S. K.; Liao, X. Z.; Zhao, Y. H.; Akhadov, E. A.; Hoffbauer, M. A.; Roop, B. J.; Jia, Q. X.; Dye, R. C.; Peterson, D. E.; Huang, S. M.; Liu, J. & Zhu, Y. T. (2004). Ultralong single-wall carbon nanotubes, *Nat. Mater.*, **3,** 10, pp. 673-676.

Zhu, L. Y.; Lu, G. H. & Chen, J. H. (2008). A generic approach to coat carbon nanotubes with nanoparticles for potential energy applications, *J. Heat Transfer-Transactions of the Asme*, **130,** 4, pp. 044502.

Zhu, L. Y.; Lu, G. H.; Mao, S.; Chen, J. H.; Dikin, D. A.; Chen, X. Q. & Ruoff, R. S. (2007). Ripening of silver nanoparticles on carbon nanotubes, *Nano*, **2,** 3, pp. 149-156.

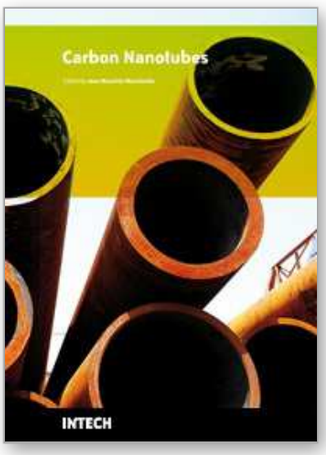


**Carbon Nanotubes**

Edited by Jose Mauricio Marulanda

ISBN 978-953-307-054-4
Hard cover, 766 pages
**Publisher** InTech
**Published online** 01, March, 2010
**Published in print edition** March, 2010

This book has been outlined as follows: A review on the literature and increasing research interests in the field of carbon nanotubes. Fabrication techniques followed by an analysis on the physical properties of carbon nanotubes. The device physics of implemented carbon nanotubes applications along with proposed models in an effort to describe their behavior in circuits and interconnects. And ultimately, the book pursues a significant amount of work in applications of carbon nanotubes in sensors, nanoparticles and nanostructures, and biotechnology. Readers of this book should have a strong background on physical electronics and semiconductor device physics. Philanthropists and readers with strong background in quantum transport physics and semiconductors materials could definitely benefit from the results presented in the chapters of this book. Especially, those with research interests in the areas of nanoparticles and nanotechnology.



INTECH
open science | open minds

**InTech Europe**
University Campus STeP Ri
Slavka Krautzeka 83/A
51000 Rijeka, Croatia
Phone: +385 (51) 770 447
Fax: +385 (51) 686 166
www.intechopen.com

**InTech China**
Unit 405, Office Block, Hotel Equatorial Shanghai
No.65, Yan An Road (West), Shanghai, 200040, China
中国上海市延安西路65号上海国际贵都大饭店办公楼405单元
Phone: +86-21-62489820
Fax: +86-21-62489821

IntechOpen